



OPEN

SUBJECT AREAS:
MATERIALS CHEMISTRY
SOFT MATERIALSReceived
2 August 2013Accepted
27 September 2013Published
15 October 2013Correspondence and
requests for materials
should be addressed to
H.M.Y. (hmyang@csu.
edu.cn)

Palladium nanoparticles deposited on silanized halloysite nanotubes: synthesis, characterization and enhanced catalytic property

Yi Zhang, Xi He, Jing Ouyang & Huaming Yang

Department of Inorganic Materials, School of Minerals Processing and Bioengineering, Central South University, Changsha 410083, China.

Palladium (Pd) nanoparticles were deposited on the surface of halloysite nanotubes (HNTs) modified with γ -aminopropyltriethoxysilane (APTES) to produce Pd/NH₂-HNTs nanocomposites. The results indicated that Pd nanoparticles were densely immobilized onto NH₂-HNTs with an average diameter of ~ 3 nm. The Pd distribution on the surface of silanized HNTs showed much more uniform, and the Pd nanoparticle size became smaller compared with those directly deposited onto HNTs without silanization. Systematic characterization demonstrated that APTES were chemically bonded onto HNTs, and further confirmed the bond formation between Pd and -NH₂ groups, which could ensure the firm deposit of Pd nanoparticles on the surface of silanized HNTs. The as-synthesized Pd/NH₂-HNTs exhibited an excellent catalytic activity in the liquid-phase hydrogenation of styrene to ethylbenzene with full conversion within 30 min. The mechanism of the deposit of Pd nanoparticles on silanized HNTs was also investigated.

Precious metals nanoparticles on catalyst supports have attracted considerable interest because they have been used in a number of catalysis applications, including transformation of organic^{1–5} and fuel cells^{6–11}. Reports indicate that the catalytic performance could be greatly enhanced by nanotube supports. Halloysite nanotube (HNT) is a typical catalyst support material. Halloysite (Al₂Si₂O₅(OH)₄·2H₂O), a hydrated layered aluminosilicate of the kaolinite group, containing octahedral gibbsite Al(OH)₃ and tetrahedral SiO₄ sheets (i.e., halloysite nanotubes), possesses a hollow cylinders formed by multiply rolled layers^{12,13}. Because of its structural features, it offers potential application as support for catalytic composites with remarkable improved mechanical properties and dispersibility^{14–17}. However, natural untreated halloysite has a very low adhesion to bond metal nanoparticles due to the absence of chemical conjunction, leading to the catalyst particles easily leaching from the support surface during the reactions.

It is well-known that the aminofunctional silanes can be applied to improve the adhesion between the metal nanoparticles and the support, thus increase the amounts of the metal particles loaded^{18–21}. In recent years, there are many literatures about the immobilization of metal nanoparticles on clay minerals with organosilane, especially for tubular aluminosilicate clay (e.g. imogolite^{22,23}, chrysotile^{24,25} and halloysite^{26–28}), which plays an important role in catalytic area. The modification of halloysite surfaces by coupling with functionalized organosilanes is applicable to the fields of enzymes immobilization^{29,30}, anti-corrosion^{31–33}, and nanocomposite materials^{14,34}.

In this paper, we reported the immobilization of palladium nanoparticles on silanized HNTs (Pd/NH₂-HNTs) with the assistance of organosilane. The Pd/NH₂-HNTs catalyst exhibits an excellent activity in the hydrogenation of styrene because of the strong synergistic interaction between palladium nanoparticles and HNTs. We investigated the interfacial characteristics of palladium, organosilane and halloysite, and its possible enhanced catalytic activity in detail.

Results

The XRD patterns of HNTs, NH₂-HNTs and Pd/NH₂-HNTs are shown in Figure 1a. For the HNTs sample, all of the observed peaks are close to the characteristic data of halloysite (JCPDS card No. 29-1487). For the NH₂-HNTs sample, all of the observed peaks are also consistent with HNTs, indicating that the existence of APTES in the

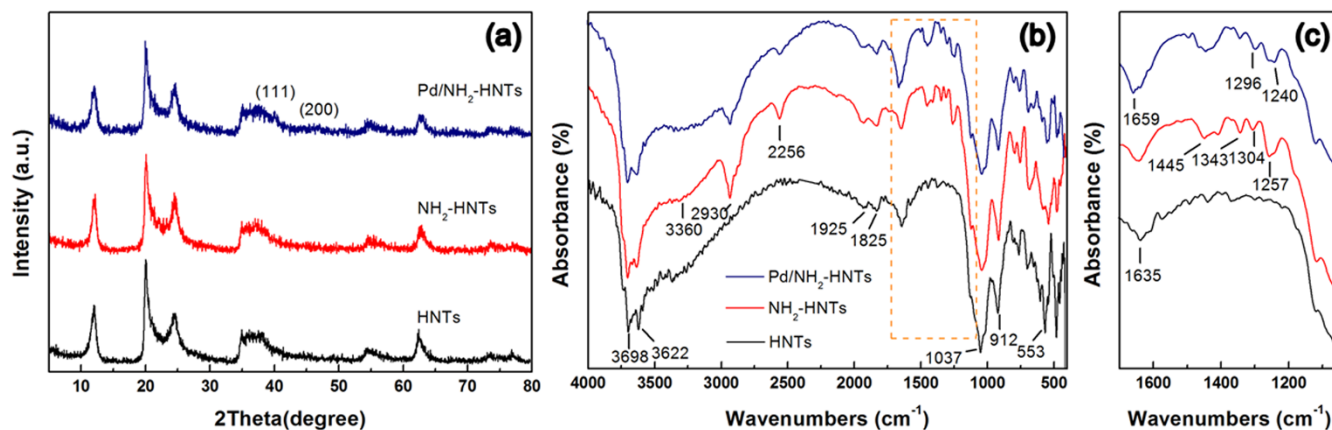


Figure 1 | Crystallization and spectra of the samples. (a) XRD patterns and (b) FTIR spectra of HNTs, NH_2 -HNTs and Pd/NH_2 -HNTs, (c) amplification of the indicated part in (b).

NH_2 -HNTs nanocomposites doesn't affect the structure of HNTs. Full range XPS spectra of samples are exhibited in Figure S1, the semiquantitative analysis of the relative atomic concentration of different elements are shown in Table S1. Si and Al are detected in both types of samples, and the concentration ratio of Si/Al is 1.46 in NH_2 -HNTs, significantly higher than the value of 1.14 in HNTs, which confirms that the silane coupling agent is present in NH_2 -HNTs. The Si in NH_2 -HNTs partly comes from the APTES. Compared with HNTs, N 1s signal is detected in NH_2 -HNTs, but the peak is not obvious especially for the sample with low APTES concentration. Those results indicate that the N species are belonging to APTES. For the Pd/NH_2 -HNTs sample, a weak peak observed at 40° , corresponding to (111) diffraction of palladium. Those results indicate that palladium salts have been reduced to metallic Pd, which is deposited on NH_2 -HNTs as nanoparticles. The characteristic peak of palladium in Pd/NH_2 -HNTs with high APTES concentration is not obvious (Figure S2), which should be due to only a partial reduction of Pd(II) to Pd(0). The crystal size of the Pd nanoparticles in Pd/NH_2 -HNTs sample calculated by the Scherrer's equation is ~ 3 nm.

The FTIR spectra of HNTs, NH_2 -HNTs and Pd/NH_2 -HNTs are shown in Figure 1b. For HNTs, the peak at 3698 cm^{-1} can be assigned to the O-H stretching vibration of the inner-surface Al-OH groups. The peak at 3622 cm^{-1} can be ascribed to the O-H stretching vibration of the inner Al-OH groups (between the interface of the Si-O tetrahedron and the Al-O octahedron). The broad band between 1633 and 3448 cm^{-1} arises from adsorbed water. The peak at 1037 cm^{-1} corresponds to the in-plane stretching vibration of the Si-O network (Si-O-Si and O-Si-O). The peak at 912 cm^{-1} is attributed to the O-H deformation vibration of inner Al-OH groups. The deformation vibration of Al-O-Si at 553 cm^{-1} is attributed to Al-O tetrahedral sheets. The Si-O-Si deformation vibration observed at 471 cm^{-1} is attributed to Si-O tetrahedral sheets.

After the functionalization of HNTs by APTES, the broad band at 3360 cm^{-1} is attributed to the N-H₂ asymmetric stretching vibration. The peak at 2930 cm^{-1} is assigned to the symmetric stretching vibration of C-H₂. The peak at 1343 cm^{-1} is attributed to the deformation (scissoring) vibration of Si-CH. The peak at 1304 cm^{-1} can be assigned the stretching vibration of C-N band. The peak at 1257 cm^{-1} is ascribed to deformation (scissoring) vibration of C-H₃. All of these observations prove the presence of the APTES in the functionalized HNTs. The signals of adsorbed water become increased with the increase of the APTES concentration. (Figure S3 & Figure S4).

After NH_2 -HNTs being assembled by PVP-Pd, some peaks have shifted and some are increased, indicating the existence of Pd in Pd/NH_2 -HNTs. The C=O stretching vibration of PVP at 1659 cm^{-1} is attributed to the interaction between PVP and metal species. The C-H₃ broad stretching band around 1257 cm^{-1} and the stretching

vibration of C-N band at 1304 cm^{-1} shift to 1240 cm^{-1} and 1296 cm^{-1} , respectively. These shifts of peaks in the Pd/NH_2 -HNTs are associated with the formation of bonds between PVP-Pd and NH_2 -HNTs.

TEM images of HNTs and Pd/NH_2 -HNTs are presented in Figure 2. The white HNTs are short cylindrical hollow tubes averaging $0.7\text{--}1.5\text{ }\mu\text{m}$ in length, with an external diameter of $50\text{--}75\text{ nm}$ and an internal diameter of $10\text{--}30\text{ nm}$ (Figure 2a). After assembly with Pd nanoparticles, the characteristic tube morphology of the original minerals have been retained (Figure 2b). According to the additional EDS spectra (Figure S5a,c, inset), compared to those deposited on HNTs without silanization ($1.0\text{ wt.}\%$, Figure S5c,d), more Pd nanoparticles ($11.3\text{ wt.}\%$) are densely dispersed on the external and internal surfaces of the NH_2 -HNTs (Figure S5a,b, Figure 2c), attributed to the amino groups on the surface of NH_2 -HNTs catching the metal colloidal more easily through coordinate bond, which is beneficial to the enhanced catalytic activity of Pd/NH_2 -HNTs. The size of Pd nanoparticle is observed as $\sim 3\text{ nm}$

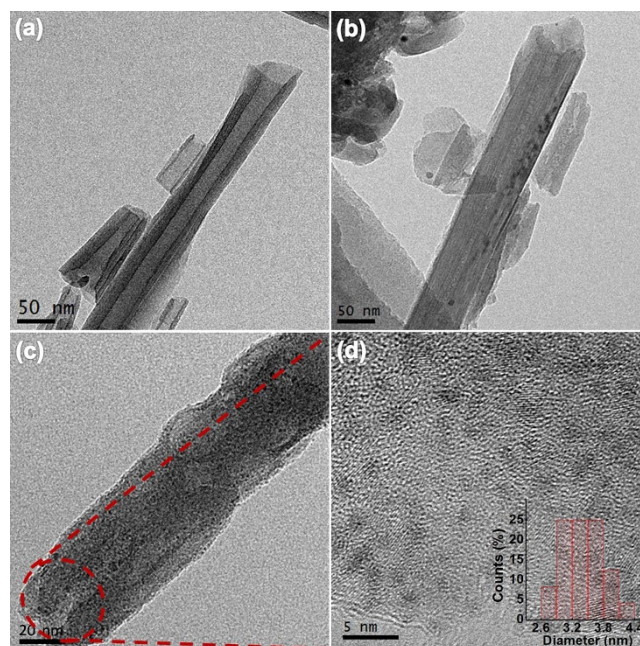


Figure 2 | Morphologies of the samples. TEM images of (a) HNTs and (b,c) Pd/NH_2 -HNTs, (d) enlargement of the indicated part in (c), inset is the particle size distribution of Pd on NH_2 -HNTs.



(Figure 2d), which shows very nice consistency with the particle size estimated by XRD.

Figure 3a shows the ^{29}Si CP/MAS NMR spectra of HNTs, NH_2 -HNTs and Pd/NH_2 -HNTs. The spectrum of HNTs indicates an obvious peak at -92 ppm, assigned to the $\text{Si}(\text{OSi})_3(\text{OAl})$ of halloysite. The spectrum of NH_2 -HNTs and Pd/NH_2 -HNTs displays two

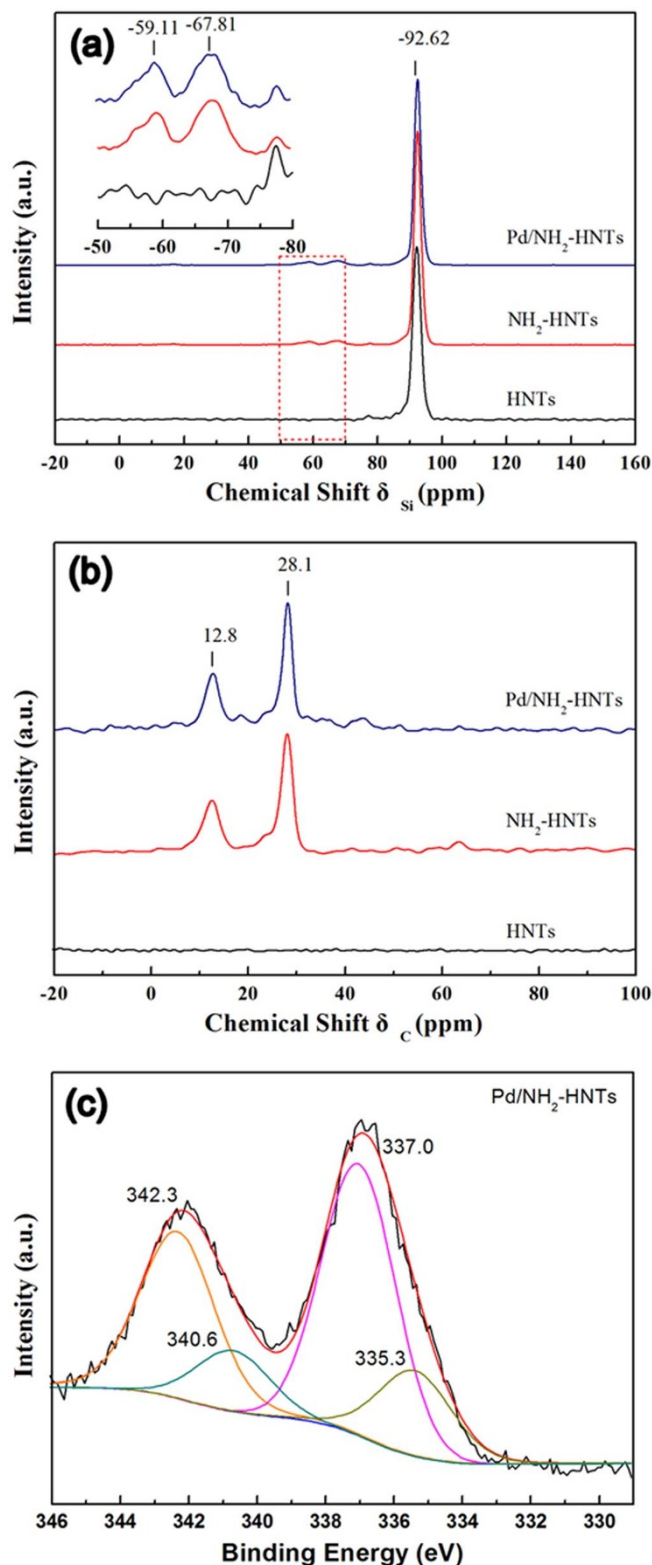


Figure 3 | Spectra analysis of the samples. (a) Solid-state ^{29}Si and (b) ^{13}C NMR spectra of HNTs, NH_2 -HNTs and Pd/NH_2 -HNTs, respectively. (c) Pd 3d XPS spectra of Pd/NH_2 -HNTs.

more resonance peaks at -65 ppm corresponding to tridentate, and at -57 ppm, attributed to bidentate. The tridentate form of Si implies that all three of the ethoxyl groups of APTES are hydrolyzed and condensed with surface hydroxyl groups of halloysite or with other hydrolyzed APTES. Observation of the bidentate form of Si means that some APTES species possess one ethoxyl (or hydroxyl) group that did not hydrolyze or condense.

Figure 3b shows the ^{13}C CP/MAS NMR spectra of HNTs, NH_2 -HNTs and Pd/NH_2 -HNTs. For HNTs, no signals are resolved by Gaussian deconvolution. For the spectra of NH_2 -HNTs and Pd/NH_2 -HNTs, the signal at 12.8 ppm is assigned to the carbon atoms at position Si-C in ethoxyl groups. The signal at 28.1 ppm is attributed to the carbon atoms at position C-C in the propyl groups, the intensities of corresponding signals become increased as the APTES concentration increased (Figure S6).

Figure 3c shows the Pd 3d spectra and their peak positions from the sample. Pd/NH_2 -HNTs has photoelectron peaks corresponding to both Pd(0) and Pd(II) species. The Pd $3d_{5/2}$ and Pd $3d_{3/2}$ electronic states for Pd(0) are observed at 335.3 and 340.6 eV, respectively. Peaks are also detected at 337.0 and 342.3 eV, corresponding to the $3d_{5/2}$ and $3d_{3/2}$ electronic states, of Pd(II) species, respectively, which suggests that the reduction process led to only a partial reduction of Pd(II) to Pd(0) for Pd/NH_2 -HNTs. As in this investigation, the atomic concentration of Pd 3d increases with increasing the atomic concentration of the N 1s (Table S1), which could be related to APTES-Pd(II) or APTES-Pd(0) complex. Figure S7a shows that Pd^{2+} is not reduced until the hydrazine hydrate is added. Based on the peak integration (Figure S7b), the proportion of Pd(0)/(Pd(0) + Pd(II)) in Pd/NH_2 -HNTs with high APTES concentration is 23.5%, lower than the Pd/NH_2 -HNTs with low APTES concentration (31.2%), indicating that the coordination between Pd(II) and APTES makes Pd(II) difficult to be reduced.

The catalytic properties of the HNTs, Pd/HNTs and Pd/NH_2 -HNTs are tested in the hydrogenation of styrene to ethylbenzene in an autoclave, as shown in Figure 4. It can be seen that the hydrogenation rate of Pd/NH_2 -HNTs is higher than that of Pd/HNTs under the same reaction conditions. Correlation of the catalytic activities of the Pd nanoparticles with their distribution indicates that a higher loading content and dispersion led to higher catalytic activity (Figure S8). Our experimental findings suggest that the surface property of the NH_2 -HNTs is beneficial to improving the dispersion and loading content, leading to a higher catalytic activity.

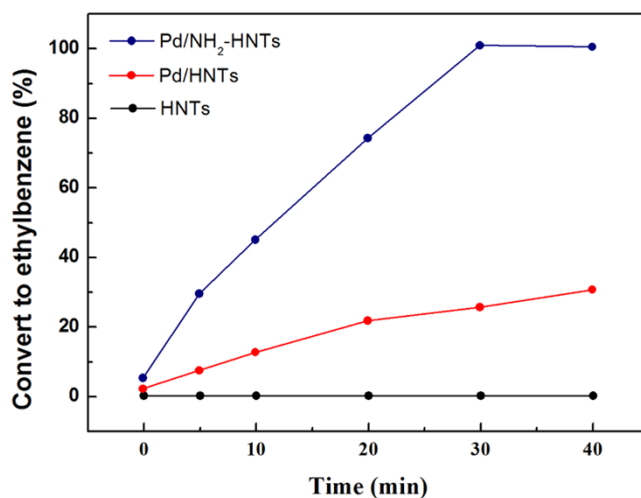


Figure 4 | Catalytic property of the samples. The change of concentration of styrene and ethylbenzene with the reaction proceeding.

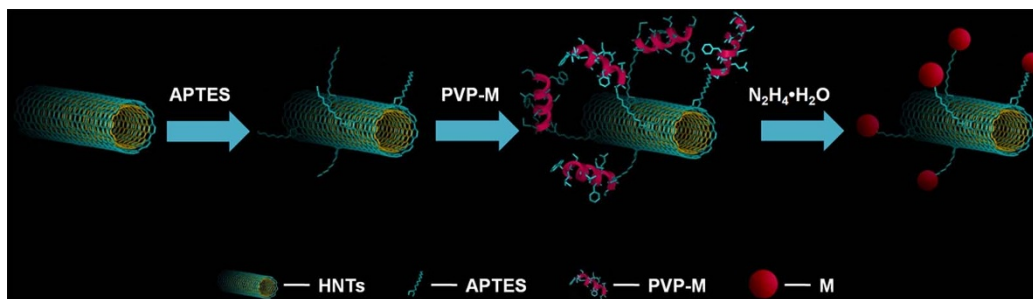


Figure 5 | Pd nanoparticles assembled on silanized HNTs. Schematic of the fabrication process for Pd/NH₂-HNTs nanocomposites.

Discussion

The present process is schematically illustrated in Figure 5. Firstly, the surface of HNTs is functionalized with -NH₂ by APTES. The functionalized HNTs possess a large number of -NH₂ groups with positive charge, and can catch the PVP-Pd²⁺ colloidal with negative charge through coordinate bonds^{35–37}. Due to the bond formation between PVP-Pd²⁺ and -NH₂ groups, most of the PVP-Pd²⁺ are combined with the -NH₂ groups. Then, the addition of hydrazine hydrate could result in the formation of Pd-NH₂ complexes; meanwhile the Pd ions are reduced by hydrazine hydrate. The bond formation between Pd and -NH₂ groups could be testified.

The peak fitting program on XPS spectra of Al 2p and Si 2p is performed to detect the possible interaction between functional APTES and HNTs^{27,38}. The XPS spectra, together with their fitting curves, are shown in Figure 6. The content of aluminol (Al-OH) at 74.8 eV on HNTs inner surface is quite low and the aluminumeoxygen (Al-O) bond is dominant in the existing forms of Al atoms. The binding energy (BE) value of Si 2p in silanol (Si-OH) is at 103.3 eV. The content of Si-OH, located at the outer side of HNTs lumens, is lower than that of siliconeoxygen (Si-O) bond (102.7 eV). When HNTs is treated with APTES, the XPS spectra of Al 2p show that the BE value of Al atom in Al-O and Al-OH are shifted to 74.6 and

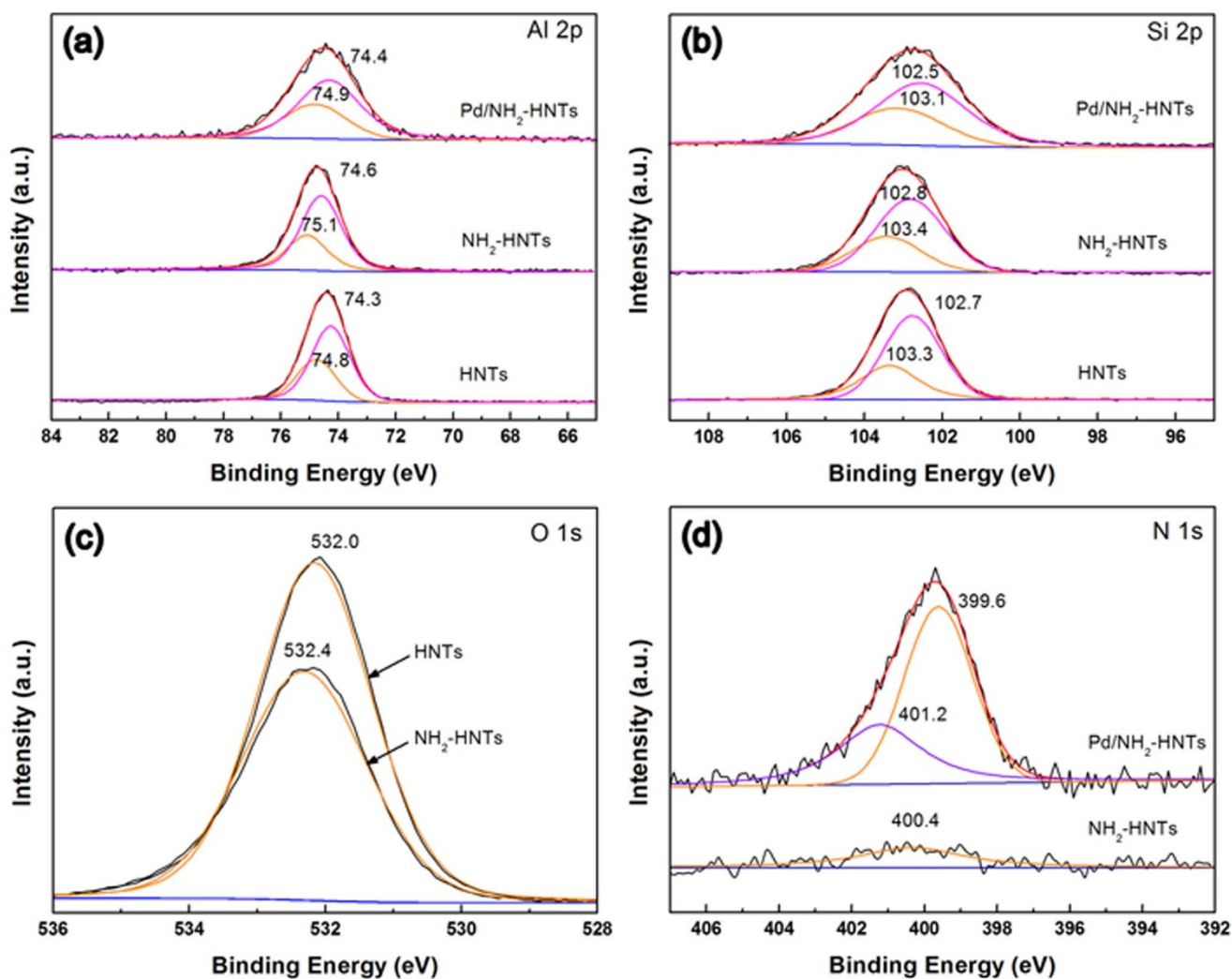


Figure 6 | XPS spectra of the samples. (a) Al 2p and (b) Si 2p and XPS spectra of HNTs, NH₂-HNTs and Pd/NH₂-HNT, (c) O 1s of HNTs and NH₂-HNTs and (d) N 1s XPS spectra of NH₂-HNTs and Pd/NH₂-HNT.



75.1 eV, respectively. According to the spectra of Si 2p, the BE value of Si in Si-OH partially moves to 103.4 eV. The other part of Si-O bonding moves to 102.8 eV. The obviously changed BE values for Al and Si atoms may be related to coupling reaction between ethoxyl groups group in APTES and hydroxyls (Al-OH and Si-OH) on HNTs. The covalently bonding between APTES and HNTs is possibly responsible for the obvious BE shifts (Figure S9). After NH₂-HNTs being assembled by PVP-Pd, the XPS spectra of Al 2p show that the BE value of Al atom in Al-O and Al-OH are shifted to 74.4 and 74.9 eV, respectively. According to the spectra of Si 2p, The BE value of Si in Si-OH partially shifted to lower binding energies with a higher value for the full width at a half-maximum (FWHM). The BE value of Si in Si-O moves to 103.1 eV. The obviously changed BE values for Al and Si atoms may be related to coupling reaction between carbonyl group in PVP-Pd and amino on NH₂-HNTs.

To prove that the APTES were chemically bonded onto HNTs, the O 1s spectra of the HNTs and NH₂-HNTs are presented in Figure 6c. As observed in Figure 6c, the intense characteristic peak that emerged at 532.0 eV corresponds well with O 1s of HNTs binding energy. After the functionalization of HNTs by APTES, the binding energy of O 1s increases to 532.4 eV, indicating that the APTES has successfully grafted on the HNTs. To further confirm the Pd nanoparticles are chemically bonded onto NH₂-HNTs, Figure 6d shows the N 1s spectra of the NH₂-HNTs and Pd/NH₂-HNTs, the peak occurred at 400.4 eV, standing for the chemical states of nitrogen in NH₂-HNTs. However, the binding energies of N 1s observed in Pd/NH₂-HNTs shifts to 401.2 eV, demonstrating the strong interaction between Pd and -NH₂ groups. The fitting line at lower binding energy (Peaks at 399.6 eV) is attributed to an N species in PVP-Pd. So, all of the above results can confirm the bond formation between the Pd and -NH₂ groups, and the functional groups can combine Pd with chemical bond, which shows an exciting prospect for immobilization of Pd.

In summary, the surface of HNTs has been functionalized with silane coupling agent, and Pd nanoparticles are then deposited on the surface of NH₂-HNTs to fabricate Pd/NH₂-HNTs composites. The distribution of Pd nanoparticles deposited on silanized HNTs are much more uniform and the particle size is smaller, compared to those deposited on HNTs without silanization. Moreover, the Pd nanoparticles deposited on NH₂-HNTs show a higher activity in the liquid-phase hydrogenation of styrene to ethylbenzene.

Methods

Material preparation. Halloysite nanotubes (HNTs) were obtained from Hunan, China. All chemicals were analytical grade and used without further purification. HNTs were pretreated via emulsion dispersion, filtering, washing with distilled water, and drying for 8 h at 313 K. (1) PVP-PdCl₂ was prepared as follows: 18 mg of sodium tetrachloride palladate (Na₂PdCl₄) was dissolved in 50 mL of methanol containing 19 mg of poly (vinyl pyrrolidone) (PVP). The solution was refluxed for 2 h until a yellowish-brown color was observed. The solution was stored in a dark bottle at 4°C for further use. (2) NH₂-HNTs nanocomposites were synthesized as follows: 4 mL of APTES was dissolved in 250 mL of dry toluene. Approximately 5 g of clay powder was added, and the suspension was dispersed ultrasonically for 30 min. Evacuation pretreatment may be carried out at this stage. The suspension was then refluxed at 120°C for 20 h under constant stirring. In the refluxing system, a calcium chloride drying tube was attached to the end to ensure a dry environment. The solid phase in the resultant mixture was filtered and extensively washed six times with fresh toluene to remove the excess organosilane, then dried overnight at 120°C for further curing. (3) PVP-Pd/NH₂-HNTs nanocomposites were synthesized as follows: 0.3 g NH₂-HNTs sample was kept in 150 mL PVP-PdCl₂ solution for 12 h and was then rinsed thoroughly with distilled water and dried at room temperature. After impregnation, the color of the sample changed from white to yellowish-brown. Finally, the sample was reduced by 60 mL of a 0.015 M alkaline solution (pH = 9.5) of hydrazine hydrate (N₂H₄·H₂O), the color of the sample changed from yellowish-brown to dark-brown, suggesting the formation of metallic palladium nanoparticles on the surface. (4) Pd/HNTs nanocomposites were synthesized as follows: 0.3 g HNTs was kept in 150 mL PVP-PdCl₂ solution for 12 h, then thoroughly washed with distilled water, and dried at room temperature. After impregnation, the color of the sample changed from white to yellowish-brown. Finally, the sample was reduced by 60 mL of a 0.015 M alkaline solution (pH = 9.5) of hydrazine hydrate (N₂H₄·H₂O), the color of the sample

changed from yellowish-brown to dark-brown, suggesting the formation of metallic palladium nanoparticles on the surface.

Characterization. The crystalline phases were identified by XRD analysis using a RIGAKU D/max-2550VB+ 18-kW powder diffractometer with Cu K α radiation (λ = 1.5418 Å). The data were collected in the scanning range 2θ = 10–80°, with a scanning speed of 2°/min. FTIR spectra were recorded using a Nicolet 5700 spectrophotometer. TEM images were obtained using a JEOL JEM-200CX instrument equipped with an energy dispersive X-ray spectroscopy (EDS) at an accelerating voltage of 200 kV. Solid state ²⁹Si MAS NMR measurements were recorded using a Bruker AMX400 spectrometer in a static magnetic field of 9.4 T at a resonance frequency of 79.49 MHz. X-ray photoelectron spectroscopy (XPS) analysis was performed on Thermo Fisher Scientific K-Alpha 1063 spectrometer equipped with an Al K α monochromator X-ray source. The test chamber pressure was maintained below 10⁻⁹ mbar during spectral acquisition. The XPS binding energy (BE) was internally referenced to the C 1s peak (BE = 284.1 eV). The catalytic hydrogenation of styrene to ethylbenzene (Figure S10) was carried out in a 300 mL stainless steel autoclave equipped with a magnetically driven impeller. For each experiment, 1 mL of styrene dissolved in 200 mL of ethanol was first charged into the autoclave reactor. Once the Pd/NH₂-HNTs were mixed inside the autoclave, hydrogen was introduced into the reactor to a set level, and the stirring rate was maintain at 60 rpm.

- Varade, D. & Haraguchi, K. Synthesis of highly active and thermally stable nanostructured Pt/clay materials by clay-mediated in situ reduction. *Langmuir* **29**, 1977–1984 (2013).
- Uppal, M. A., Kafizas, A., Ewing, M. B. & Parkin, I. P. The room temperature formation of gold nanoparticles from the reaction of cyclohexanone and auric acid; a transition from dendritic particles to compact shapes and nanoplates. *J. Mater. Chem. A* **1**, 7351–7359 (2013).
- Cornelio, B. *et al.* Palladium nanoparticles on carbon nanotubes as catalysts of cross-coupling reactions. *J. Mater. Chem. A* (2013).
- Zinovyeva, V. A., Vorotyntsev, M. A., Bezverkhy, I., Chaumont, D. & Hierso, J.-C. Highly dispersed palladium-polyppyrole nanocomposites: in-water synthesis and application for catalytic arylation of heteroaromatics by direct C-H bond activation. *Adv. Funct. Mater.* **21**, 1064–1075 (2011).
- Wang, Z. L., Yan, J. M., Wang, H. L., Ping, Y. & Jiang, Q. Pd/C synthesized with citric acid: an efficient catalyst for hydrogen generation from formic acid/sodium formate. *Sci. Rep.* **2**, 598 (2012).
- Fujigaya, T. & Nakashima, N. Fuel cell electrocatalyst using polybenzimidazole-modified carbon nanotubes as support materials. *Adv. Mater.* **25**, 1666–1681 (2013).
- Sridhar, V. *et al.* Defect-engineered three-dimensional graphene-nanotube-palladium nanostructures with ultrahigh capacitance. *ACS Nano* **6**, 10562–10570 (2012).
- Claussen, J. C. *et al.* Nanostructuring platinum nanoparticles on multilayered graphene petal nanosheets for electrochemical biosensing. *Adv. Funct. Mater.* **22**, 3399–3405 (2012).
- Oh, H.-S. & Kim, H. Efficient synthesis of Pt nanoparticles supported on hydrophobic graphitized carbon nanofibers for electrocatalysts using noncovalent functionalization. *Adv. Funct. Mater.* **21**, 3954–3960 (2011).
- Morgan, R. D., Salehi-khojin, A. & Masel, R. I. Superior formic acid oxidation using carbon nanotube-supported palladium catalysts. *J. Phys. Chem. C* **115**, 19413–19418 (2011).
- Yang, X. D. *et al.* A direct borohydride fuel cell with a polymer fiber membrane and non-noble metal catalysts. *Sci. Rep.* **2**, 567 (2012).
- Joussein, E. *et al.* Halloysite clay minerals - a review. *Clay Miner.* **4**, 383–426 (2005).
- Guimarães, L., Enyashin, A. N., Seifert, G. & Duarte, H. A. Structural, electronic, and mechanical properties of single-walled halloysite nanotube models. *J. Phys. Chem. C* **114**, 11358–11363 (2010).
- Zhang, Y. & Yang, H. M. Halloysite nanotubes coated with magnetic nanoparticles. *Appl. Clay Sci.* **56**, 97–102 (2012).
- Zhang, Y. & Yang, H. M. Co₃O₄ nanoparticles on the surface of halloysite nanotubes. *Phys. Chem. Miner.* **39**, 789–795 (2012).
- Zhang, Y. & Yang, H. M. ZnS/halloysite nanocomposites: synthesis, characterization and enhanced photocatalytic activity. *Funct. Mater. Lett.* **6**, 1350013 (2013).
- Zhao, Y. F., Abdullayev, E., Vasiliev, A. & Lvov, Y. Halloysite nanotubule clay for efficient water purification. *J. Colloid Interface Sci.* **406**, 121–129 (2013).
- Datta, K. K. R., Acharia, A. & Eswaramoorthy, M. Aminoclay: a functional layered material with multifaceted applications. *J. Mater. Chem. A* **1**, 6707–6718 (2013).
- Yuan, P. *et al.* Functionalization of halloysite clay nanotubes by grafting with γ -aminopropyltriethoxysilane. *J. Phys. Chem. C* **112**, 15742–15751 (2011).
- Yang, H. M., Li, M., Fu, L. J., Tang, A. D. & Mann, S. Controlled assembly of Sb₂S₃ nanoparticles on silica/polymer nanotubes: insights into the nature of hybrid interfaces. *Sci. Rep.* **3**, 1336 (2012).
- Li, C. C., Fu, L. J., Yang, J. O. & Yang, H. M. Enhanced performance and interfacial investigation of mineral-based composite phase change materials for thermal energy storage. *Sci. Rep.* **3**, 1908 (2013).



22. Ma, W., Otsuka, H. & Takahara, A. Poly(methyl methacrylate) grafted imogolite nanotubes prepared through surface-initiated ARGET ATRP. *Chem. Commun.* **47**, 5813–5815 (2011).
23. Bottero, I. *et al.* Synthesis and characterization of hybrid organic/inorganic nanotubes of the imogolite type and their behaviour towards methane adsorption. *Phys. Chem. Chem. Phys.* **13**, 744–750 (2011).
24. Liu, H. F., Peng, T. J., Ma, G. H., Sun, H. J. & Hua, H. L. Simple chemical solution coating and gas sensing properties of α -Fe₂O₃/chrysotile fibrous composites. *Appl. Surf. Sci.* **258**, 4866–4870 (2012).
25. Lourenço, M. P., Oliveira, C. d., Oliveira, A. F., Guimarães, L. & Duarte, H. A. Structural, electronic, and mechanical properties of single-walled chrysotile nanotube models. *J. Phys. Chem. C* **116**, 9405–9411 (2012).
26. Tan, D. Y. *et al.* Natural halloysite nanotubes as mesoporous carriers for the loading of ibuprofen. *Micropor. Mesopor. Mater.* **179**, 89–98 (2013).
27. Zhu, H., Du, M. L., Zou, M. L., Xu, C. S. & Fu, Y. Q. Green synthesis of Au nanoparticles immobilized on halloysite nanotubes for surface-enhanced raman scattering substrates. *Dalton Trans.* **41**, 10465–10471 (2012).
28. Hashemifard, S. A., Ismail, A. F. & Matsuura, T. Mixed matrix membrane incorporated with large pore size halloysite nanotubes (HNT) as filler for gas separation: Experimental. *J. Colloid Interface Sci.* **359**, 359–370 (2011).
29. Zhai, R. *et al.* Immobilization of enzyme biocatalyst on natural halloysite nanotubes. *Catal. Commun.* **12**, 259–263 (2010).
30. Zhai, R. *et al.* Chitosan-halloysite hybrid-nanotubes: Horseradish peroxidase immobilization and applications in phenol removal. *Chem. Eng. J.* **214**, 304–309 (2013).
31. Abdullayev, E. & Lvov, Y. Clay nanotubes for corrosion inhibitor encapsulation: release control with end stoppers. *J. Mater. Chem.* **20**, 6681–6687 (2010).
32. Shchukin, D. G. *et al.* Active anticorrosion coatings with halloysite nanocontainers. *J. Phys. Chem. C* **112**, 958–964 (2008).
33. Fix, D., Andreeva, D. V., Lvov, Y. M., Shchukin, D. G. & Möhwald, H. Application of inhibitor-loaded halloysite nanotubes in active anti-corrosive coatings. *Adv. Funct. Mater.* **19**, 1720–1727 (2009).
34. Wang, L., Chen, J. L., Ge, L., Rudolph, V. & Zhu, Z. H. Halloysite nanotube supported Ru nanocatalysts synthesized by the inclusion of preformed Ru nanoparticles for preferential oxidation of CO in H₂-rich atmosphere. *J. Phys. Chem. C* **117**, 4141–4151 (2013).
35. Besteman, K., Zevenbergen, M. A. G., Heering, H. A. & Lemay, S. G. Direct observation of charge inversion by multivalent ions as a universal electrostatic phenomenon. *Phys. Rev. Lett.* **93**, 170802 (2004).
36. Cui, Y., Wei, Q. Q., Park, H. K. & Lieber, C. M. Nanowire nanosensors for highly sensitive and selective detection of biological and chemical species. *Science* **293**, 1289–1292 (2001).
37. Peng, C., Sylvia, H. Y. Lo., Wan, C. C. & Wang, Y. Y. Study of the adsorptive behavior of Pd/PVP nanoparticles and its interaction with conditioner in electroless copper deposition. *Colloids Surf. A* **308**, 93–99 (2007).
38. Lei, Y. D., Tang, Z. H., Zhu, L. X., Guo, B. C. & Jia, D. M. Functional thiol ionic liquids as novel interfacial modifiers in SBR/HNTs composites. *Polymer* **52**, 1337–1344 (2011).

Acknowledgments

This work was supported by the National Science Fund for Distinguished Young Scholars (51225403), the Specialized Research Fund for the Doctoral Program of Higher Education (20120162110079) and the Scholarship Award for Excellent Doctoral Student granted by Ministry of Education (1343-76140000026).

Author contributions

H.M.Y. conceived the project and wrote the final paper. Y.Z. wrote initial drafts of the work. Y.Z. designed the experiments, synthesized and characterized the materials. X.H., Y.Z. and J.O.Y. analyzed the XPS spectra. All authors discussed the results and commented on the manuscript.

Additional information

Supplementary information accompanies this paper at <http://www.nature.com/scientificreports>

Competing financial interests: The authors declare no competing financial interests.

How to cite this article: Zhang, Y., He, X., Ouyang, J. & Yang, H.M. Palladium nanoparticles deposited on silanized halloysite nanotubes: synthesis, characterization and enhanced catalytic property. *Sci. Rep.* **3**, 2948; DOI:10.1038/srep02948 (2013).



This work is licensed under a Creative Commons Attribution-NonCommercial-NoDerivs 3.0 Unported license. To view a copy of this license, visit <http://creativecommons.org/licenses/by-nc-nd/3.0>